Int. J. Multiphase Flow Vol. 18, No. 3, pp. 371–395, 1992
Printed in Great Britain

0301-9322/92 $5.00 + 0.00
Pergamon Press Ltd

SIMULTANEOUS VELOCITY MEASUREMENTS OF BOTH COMPONENTS OF A TWO-PHASE FLOW USING PARTICLE IMAGE VELOCIMETRY

Y. A. HASSAN, T. K. BLANCHAT, C. H. SEELEY JR and R. E. CANAAN
Department of Nuclear Engineering, Texas A&M University, College Station, TX 77843, U.S.A.

(Received 21 March 1991; in revised form 11 November 1991)

Abstract—The study undertaken is an examination of a two-phase dispersed air bubble mixing flow within a rectangular vessel. The technique of particle image velocimetry (PIV) is utilized in order to obtain non-invasive velocity measurements of the resulting bubbly flow field and its induced effects upon a surrounding liquid medium. The method provides not only a visualization of the various patterns and structures of a given flow field, but also yields quantitative full-field instantaneous velocity data from both phases of a two-phase system in a concurrent manner. PIV is a rapidly advancing flow visualization technique in which the instantaneous velocity profile of a given flow field is determined by photographically recording tracer particle and/or bubble images within the flow at discrete instances in time, and then conducting computational analysis of the digitized data. The use of developed analysis algorithms, which perform a point-by-point matching of particle and bubble images from one digital image frame to the next, subsequently allows reconstruction of the respective instantaneous velocity profiles. The ability to simultaneously measure the velocity fields of both components of a two-phase flow is an important contribution toward the goal of developing improved correlations for flow regime determination as well as improved model for key two-phase flow parameters such as the interfacial drag. In this work, results were obtained which indicate that the described PIV method is an effective tool in the study of the specific interactions which occur between components in a wide variety of multiphase systems.

Key Words: two-phase flow, flow visualization, bubbly flow, particle image velocimetry

1. INTRODUCTION

The objective of the following study was to apply recent advances and improvements in the technique of particle image velocimetry (PIV) to the full-field non-invasive analysis of a two-phase fluid flow system in such a manner that both components of the two-phase system could be experimentally quantified. This work invoked the PIV flow visualization method in order to obtain qualitative and quantitative velocity data for a rising dispersed air bubble field and a subsequently affected surrounding liquid medium within a transparent rectangular enclosure. The ability to simultaneously quantify both components of simple two-phase flows not only provides insight into the determination of the heat transfer and thermal hydraulic stresses associated with multiphase systems, but also contributes directly towards the goal of better understanding the fundamentals of two-phase flows and the ability to quantify such two-phase flow characteristics as void fraction, relative component velocities and interfacial drag.

Analytical solutions are difficult to obtain for most complex geometry single-phase flows. Such solutions are further complicated when considering flows consisting of more than one phase. Attempts to accurately model such flows through the use of empirical correlations have been employed; however, the effectiveness of such methods is limited by the availability of reliable high-quality experimental data from similar flow fields which provide a basis for the modeling. The ability of PIV, in conjuction with advanced image processing techniques, to capture whole-field instantaneous velocity profile data of a non-invasive nature thus provides a powerful tool in the analysis of single- and two-phase flows alike.

PIV is a flow visualization technique which allows the instantaneous measurement of quantitative velocity vectors over a full flow field in such a manner that the flow field itself remains completely undisturbed. This is in sharp contrast to such commonly used methods as hot wire or film anemometry in which velocity data is obtained for a fluid in motion by insertion of a hot wire probe

into the flow field at a given point. In addition to the intrusive drawbacks of such a technique, quantitative information can only be obtained at a single point for a given measurement; hence, many measurements are required for the generation of full-field velocity profiles. Laser Doppler anemometry [LDA; also referred to as laser Doppler velocimetry (LDV)] is a relatively more sophisticated technique in which local fluid velocities are measured non-invasively; however, as is the case with hot wire methods, LDA is limited by the fact that in order to obtain a full-field profile of a given flow regime, multiple measurements must be made at various points throughout the flow and simultaneously as well if the flow is unsteady. Various other techniques have been utilized previously in order to provide such full-field capabilities, namely methods of flow visualization such as smoke wires, by tracers and Schlieren photography (Van Dyke 1982). However, from a fluid mechanical point of view, information obtained from such visualization methods is largely considered to be based upon qualitative rather than quantitative foundations (Adrian & Landreth 1988). As a direct result of the drawbacks associated with many of the previously discussed methodologies, the technique of PIV has emerged and advanced to such an extent as to overcome some of the limitations of these traditional measurement methods. Thus, the primary advantages associated with PIV lie in the non-invasive nature of the measurements and in the full-field velocity profile generated from a single measurement.

The fundamental methodology employed in *traditional* PIV is relatively straightforward and actually rather simple in principle. The output of a pulsed or chopped high energy laser is directed through a cylindrical lens system which shapes the resulting beam into a thin planar sheet of high intensity laser light. This sheet of light is subsequently aligned and directed through the flow of interest parallel to the two-dimensional flow streamlines. Since the flow itself is seeded with neutral density light scattering particles or in this case with rising dispersed air bubbles as well as tracer particles, the incident planar sheet of laser light undergoes scattering to the viewing plane where images of the scattering seeds (bubbles or micron sized particles) may be captured on some sort of conventional photographic medium. A subsequent laser pulse is emitted a short time later relative to the flow velocity and the seed images are again captured at their new locations corresponding to the flow streamlines. The resulting doubly exposed photographic medium contains multiple randomly distributed images which represent the locations of the seeds following the flow at two discrete instances in time. The analysis of the resulting image requires measurement of the separation distance between successive seed images such that when combined with the known temporal separation, the desired velocity vectors may be determined. The great majority of previous studies conducted utilizing PIV methods have relied primarily upon opto-mechanical techniques in order to accomplish this task. A commonly used method involves the well-known Young's fringe/fast Fourier transform (FFT) approach described throughout the literature (Simpkins & Dudderar 1978; Adrian 1986a). However, as a result of rapidly advancing developments in digital image processing, many investigators have elected to forego reliance upon such opto-mechanical techniques in favor of direct digitization methods in which a series of *separate* flow image "snap shots" are captured in sequence, directly digitized and subsequently analyzed in a completely digital manner as well. Digital image capture in two or more separate image frames avoids much of the complexities associated with photographic image processing as well as directional ambiguities which arise concerning which seed image was captured first in a single doubly-exposed photographic frame (Adrian 1986b; Lourenco & Krothapalli 1987).

Techniques of cross correlation appear aptly suited for the determination of a given seed's displacement between two temporally separate digital image frames and a variety of cross correlation approaches have been proposed and implemented. Several cross correlation methods involve interrogation of two sequentially captured digital image frames in terms of smaller subgrid regions in which the average displacment and hence average velocity of the seeds in the subgrid region is determined (Kimura & Takamori 1986; Landreth & Adrian 1988). This paper describes a spatial cross correlation technique, whereby instantaneous velocities are found on a point-by-point basis (Yamamoto *et al.* 1989); in other words, velocity vectors are determined for each seed's displacement at the exact spatial location of the given seed in the image frame. Such a point-by-point approach is often preferred over methods which calculate local average velocities within a subgrid image region, since errors associated with the averaging process itself are eliminated.

In the analysis which follows, the authors of this work have utilized a direct digitization PIV cross correlation technique in which a series of 10 flow image "snap shots" are captured in sequence, directly digitized and subsequently evaluated with a point-by-point digital analysis algorithm which determines the resulting velocity field. It has been demonstrated that the developed PIV technique is capable of detailed quantitative velocity measurements in a wide variety of *single-phase* flow regimes (Hild 1989; Canaan 1990).

A topic of much greater interest concerns the specific *interactions* which occur between the components of a multiphase system. In order to fully characterize such a flow, the velocity fields of both components of a two-phase bubbly flow must be determined concurrently. This requires the simultaneous imaging and analysis of a fluid flow which contains both light scattering neutral density particles which describe the liquid flow behavior as well as bubbles which characterize the gaseous flow component. Gas agitated mixing flows are of interest in numerous practical engineering applications and are extensively used in chemical and metallurgical processing industries. Additionally, such a geometry provides a simple starting point in which basic two-phase interaction phenomena may be studied. Typically, the fluid flows in such vessels are buoyancy induced, generally turbulent and two- or three-dimensional (Salcudean & Lai 1988). Similar geometries have been utilized in single point measurement studies; however, applications involving full-field measurement techniques are rare. Experiments have been conducted in which full-field two-dimensional velocity measurements of a gas injection mixing flow were taken using a 256 × 256 pixel resolution CCD video camera in addition to a digital cross correlation analysis routine (Uemura *et al.* 1990). However, regions of the flow field through which the bubbles themselves passed were purposely excluded from the analysis due to complications involved in the digital determination of seed particle correspondence. Thus, application of full-field digital methods in the quantitative analysis of both flow components directly is currently a unique feature of this analysis.

In order to accomplish this objective the developed PIV method was applied to a simple two-phase flow regime. This regime was created within a transparent rectangular enclosure which contained an air inlet flow line terminating in a vertically positioned needle and syringe arrangement. The gaseous (air) component of the two-phase system was introduced via the flow line into mineral oil seeded with polystryene spheres. Images of the rising bubbles periodically produced at the needle outlet and their induced effects upon the surrounding seeded liquid component were sequentially recorded in multiple image frames. Following image acquisition and storage, the full-field velocity vectors of both bubbles and particles were determined on a point-by-point basis using developed algorithms which: find and define the seed images; determine corresponding seed image pairs between any two successively acquired separate image frames within a 10-frame sequence; and, finally, construct the corresponding two-dimensional instantaneous velocity vector field for both the gaseous and liquid flow components.

2. EXPERIMENTAL APPARATUS AND METHODOLOGY

2.1. General methodology

Through the utilization of the experimental arrangement shown in figure 1, the techniques of PIV were applied to the analysis of a two-phase dispersed air bubble flow in which the surrounding working fluid was a heavy mineral oil. As can be seen in figure 1, the output of a high energy pulse Nd:YAG laser was directed through a series of three plano-convex cylindrical lenses which shaped the resulting beam into a thin planar sheet of laser light. This sheet of light was aligned and diverted into a rectangular transparent enclosure in which a vertically mounted syringe and needle arrangement was centered. The alignment of the light plane in this case was adjusted such that the laser sheet illuminated an area of the tank immediately above the vertically positioned needle and air inlet. In order to quantify the velocity fields of both components of a two-phase bubbly flow simultaneously, both the liquid and gaseous phases must be appropriately "seeded". The air bubbles produced at the needle exit served as a natural seeding for the gaseous component, whereas micron-sized tracer particles enabled quantification of the liquid. The working fluid was a heavy mineral oil of sp. grav. = 0.878 (at 25°C) and kinematic viscosity 69.0 CST (at 40°C), seeded with

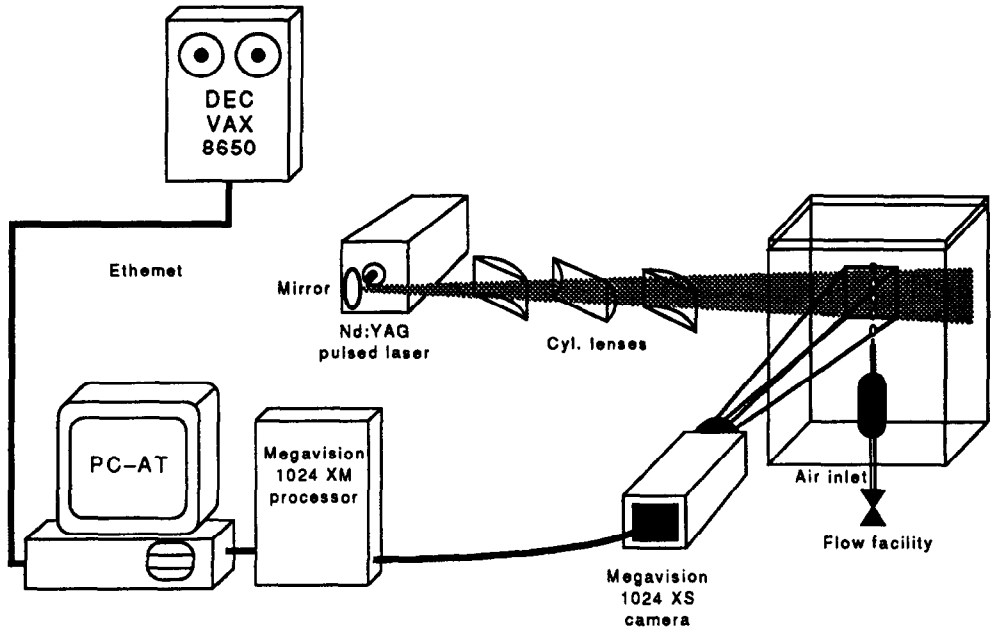

Figure 1. Experimental arrangement for the two-phase system.

70 μm (sp. grav. = 1.02) plastic spheres. The gaseous component of the flow was created in the form of millimeter-sized air bubbles produced periodically at the tip of a 27-gauge surgical needle. Transparent mineral oil was employed as the working fluid in order to slow the rise of the air bubbles, such that a series of 10 image frames would effectively record the rising bubbles as well as their subsequent influence on the seeded liquid. Additionally, the large kinematic viscosity of the oil was effective in maintaining the rising air bubbles within a two-dimensional planar viewing area.

Since the flow itself was seeded with both dispersed air bubbles and tracer particles, the incident planar sheet of laser light underwent scattering and reflection perpendicular to the viewing plane where images of the rising bubbles and particles were captured using an advanced imaging system. Subsequent laser pulses were emitted after a time delay of 150 ms and such seed images were again captured at their new locations. Typically a series of 10 image frames are captured and constitute a single data set. Several data sets of flows produced within the described arrangement were taken and subsequently evaluated. The primary distinctive components of the experimental setup are the laser and optical arrangement, the flow facility itself and the image acquisition and analysis hardware/software. Each of these components is, respectively, discussed in detail as follows.

2.2. Laser and optical arrangements

The laser used in this study was a Spectra-Physics DCR-3G Nd:YAG high energy pulsed laser. The laser is calibrated at a peak energy output of over 1.0 J per pulse for the primary wavelength of 1064 nm infrared. The pulse duration itself is 8 ns, giving rise to a peak pulse power of over 125 MW. The primary benefit of such a high energy coherent pulsed light source revolves around the relative ease with which such a laser beam may be focused into a thin sheet of intense light as well as the ability to "freeze" particle motion such that instantaneous distinct bubble images may be captured (Dudderar *et al.* 1988). The system of mirrors and lenses employed in this experiment were designed to expand the initial 7 mm circular Gaussian laser emission into an expanding light sheet of approx. 1 mm in thickness and 4 cm in width at the camera viewing plane. Problems were initially encountered due to early experiments with water, which has a large absorption cross section for near-infrared light. However, utilization of a frequency doubling

crystal to convert the 1064 nm light to 532 nm (green) light proved highly successful in eliminating this concern. Such a conversion however significantly reduces the maximum energy output at 532 nm to approx. 400 mJ; nevertheless, the compensation of increased camera sensitivity at this wavelength and the virtual elimination of absorption make up for this loss of light intensity (Hild 1989).

2.3. The flow facility

The flow container in which the dispersed air bubbly flow fields were introduced was an open-top rectangular enclosure with a square base fabricated from 0.3175 cm glass sheets. The tank measured 17.5 cm on a side and 26.0 cm in depth and was filled with the working fluid up to a height of 21.0 cm. The bubbly flow produced was introduced via an air inlet flow line into the seeded liquid environment at an approximate volumetric flow rate of 25 mm^3/s. The two-dimensional area of interest within the flow field was illuminated by expanding the emitted circular laser beam into a sheet of laser light and subsequently passing the light plane laterally through the enclosure's side wall. The formation of non-collapsing air bubbles on the free surface of the oil within the flow container would have significantly distorted the entering laser light plane had it been passed vertically through the free surface rather than laterally through the vessel's side wall. Several sets of successive digital image frames were acquired of the generated flow field in a 25 × 25 mm area immediately above the tip of the bubble-producing needle, as seen in figure 1. The horizontal and vertical locations of the image plane within the flow facility may be altered as desired such that images over a large flow field can be acquired. This was accomplished by mounting the camera imaging device on a horizontal translator while positioning the glass tank on a jack of adjustable height.

2.4. Image acquisition

Image acquisition was accomplished in this experiment through the use of a 1024 XS vidicon tube camera. This system is capable of providing a resolution of 1024 lines of 1024 picture elements (square pixels) with 8 bit or 256 gray level discrimination (Hassan *et al.* 1990). A Teltron 9800 HR TV camera tube installed in the 1024 XS provides high resolution images in addition to increased sensitivity to incoming light in the 532 nm range.

The vidicon camera system is operated in conjunction with the 1024 XM imaging unit, which converts analog camera signals into digital output in which subsequent interpretation and manipulation of image data may be accomplished. A synchronization circuit between the pulsed laser and imaging system allow the digitization and storage of up to 10 frames of image data with a time separation of 150 ms between successive frames. The time separation limit is due to the sampling frequency of the analog-to-digital converter at the camera interface. Also utilized in conjuction with the 1024 XM unit is a PC-AT compatible which operates the interfacing software associated with the image acquisition sytem. Additionally, the PC is used to permanently store image data acquired by the 1024 XS camera to either hard disk or floppy, from which subsequent transferal of data to a mainframe system is undertaken in order to implement the various developed numerical algorithms with the actual fluid mechanical analysis of the data.

2.5. Image analysis

Once a set of picture image data has been digitally captured and stored utilizing the techiques previously described the net result is a succession of 10 sequentially recorded image frames depicting the motion of tracer particles or bubbles at discrete instances in time within a given flow field. In order to accomplish the ultimate objective of obtaining the full-field quantitative velocity profile of the flow, a series of image analysis steps must be further undertaken. The analysis of the resulting images requires measurement of the separation distances between corresponding

seed images in successive image frames such that when combined with the known temporal separation (Δt), the desired velocity vectors may be determined, i.e.

$$V_i = \frac{\sqrt{\Delta x_i^2 + \Delta y_i^2}}{\Delta t}, \quad [1]$$

where

Δx_i = horizontal (x) displacement of seed i between successive images,
Δy_i = vertical (y) displacement of seed i between successive images,
Δt = time separation between successive image capture

and

V_i = instantaneous velocity magnitude of seed i.

Thus, given the spatial displacement of the recorded seed images, the velocity of the particle or bubble is easily determined. However, the challenge of PIV analysis is not that of determining seed spatial separation *per se*, but rather one of *first* establishing seed *correspondence* between image frames such that the actual displacement may be measured. This is the fundamental goal of all digital analysis algorithms, regardless of the methodologies upon which the algorithms are based.

Once the picture image data for a set of 10 image frames have been transferred to the mainframe network, a series of three numerical image analysis algorithms are subsequently implemented in order to conduct a point-by-point digital analysis which results in the full-field instantaneous velocity profile. The three coded routines which are utilized in order to accomplish this task, respectively, perform the following operations: (a) conduct a preliminary analysis of the image data including threshold and "spot" determination; (b) the actual point-by-point matching of spots from one frame to the next; (c) post-processing or "cleaning"; and (d) the graphical plotting of the instantaneous frame-by-frame velocity vectors.

The first step in the image analysis process is to find and label seed spots. A program first performs gray level thresholding on the image, then conducts a line-by-line search in order to determine whether a given pixel is in itself a particle (or bubble) spot or whether it belongs to larger group of pixels which make up a particle spot. This is accomplished by comparing each encountered pixel against its neighboring or adjacent pixels. If any one of these neighboring pixels has already been defined to be part of another particle or bubble spot, then the current pixel of interest is subsequently included in that spot. If none of the previous neighbors is a part of any spot and the current pixel does not represent a background value, then a new spot is in turn created. This is basically a pixel connectivity algorithm. In addition to finding and defining individual spots, this routine also determines the area of each spot, the corresponding x and y centroids, and the average gray level of each spot. The spot tracking routine uses the spot centroid and area in matching the spots from frame to frame.

The next step in the analysis is to accurately correlate the spot between successive frames of data. Several cross correlation methods involve interrogation of two sequentially captured digital image frames in terms of smaller subgrid regions in which an average displacement and hence average velocity of all the seeds within the subgrid region is determined. The spatial correlation method implemented in the analysis of experimental data taken in this study however, is one in which the instantaneous velocites are obtained on a *point-by-point* basis rather than one involving vector averaging over a given subregion (Hassan *et al.* 1991). The vectors produced are actually a temporal average between the two frames, however, the time step is small enough to allow the use of the term instantaneous. In other words, velocity vectors are determined for each seed's displacement at the exact spatial location of the seed within the image frame. Such a point-by-point approach is often preferred over methods which calculate local average values within a subgrid image region since errors associated with the averaging process are eliminated. For instance, if the subregion in which the cross correlation is to be performed is chosen to be excessively large, the determined average velocity is an average over a region of possible large velocity variation and, hence, the measured velocity will be unrepresentative of each individual seed's velocity (Kiritsis 1989). The spatial point-by-point correlation routine implemented in this work is based upon those found in

the literature (Yamamoto *et al.* 1989) and was subsequently adapted and modified for implementation with the current experimental methods.

The fundamental assumption upon which the method is based revolves around the fact that every seed within an image frame is part of a specific characteristic group consisting of other *nearby* seeds such that a unique local seed pattern or distribution exists. As the seeds travel with the flow, this specific distribution pattern is essentially held intact over two discrete instances in time provided the temporal separation between the two points is small compared to the rate at which the surrounding flow itself is changing. Thus, if two sequential digital images are acquired with a sufficiently small Δt (properly chosen value depends upon the timescale of the given flow), correspondence for a given seed over the two image frames may be determined by assuming that the relative positions of other seeds with respect to the seed of interest have undergone little variation within the specified time interval. The degree of correspondence between seeds in separate frames is quantitatively measured by calculating a cross correlation coefficient for each possible candidate seed pair. The specific seed in image frame 2 which has a pattern of surrounding seeds which most closely resembles a similar pattern about a given seed in frame 1 will possess the largest cross correlation coefficient and hence have the highest probability of being the same seed.

This process may be further described with reference to figure 2, which depicts a portion of a 1024 × 1024 pixel field containing representative image data for two successively acquired frames (frames 1 and 2, respectively) separated by a known Δt. In addition to defining and labeling of spots using a preliminary analysis routine, the pixels representing a spot are converted to a binary format in which all object pixels have gray level 1 and background pixels are represented by 0. A square candidate subregion is created in frame 1 which is centered upon the centroid pixel of a given spot to be correlated. In this case a candidate subregion of size 7 × 7 pixels is centered on the centroid of spot A (pixel location 25,25). After a time Δt, the spot in frame 1 have shifted a spatial distance proportional to the local velocity field. In this example case the flow is up and to the right and all spots in frame 2 have subsequently shifted in that direction. The next step is to locate the same square candidate subregion applied in frame 1 to an *identical position* in frame 2 (i.e. centered at pixel location 25,25). This identical subregion location in frame 2 is represented by a broken line. The seed spots which exist within this broken line square are the candidate spots for correspondence to spot A found in frame 1. Thus, it can be seen that an absolutely crucial parameter in this process is the specification of the size of the square candidate subregion. It must be chosen to be sufficiently large such that the seed spot undergoing correlation remains within the square subregion in both frames when the subregion position in frame 2 is identical to its position in frame 1. If this square is not sufficiently large such that it exceeds the maximum expected

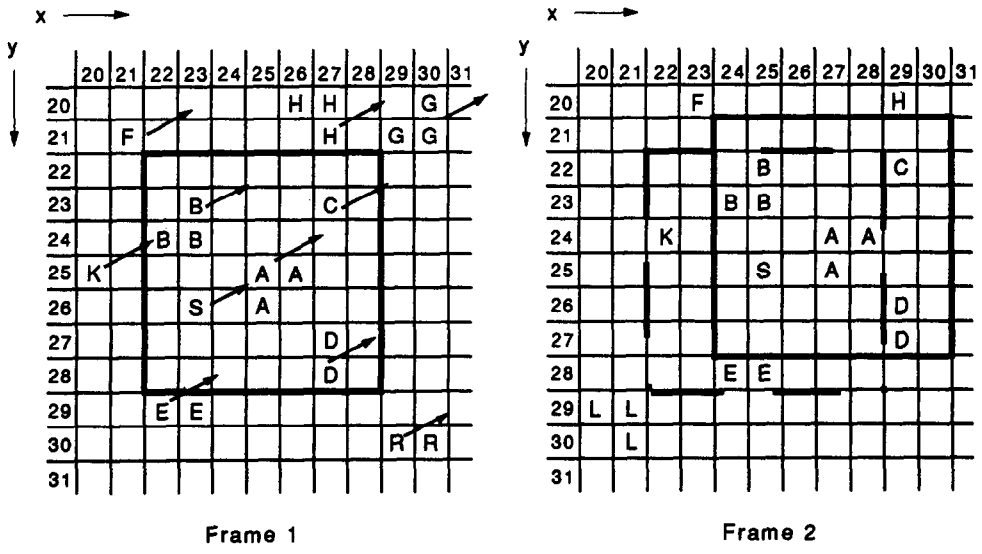

Figure 2. Illustration of the cross correlation technique.

seed displacement anywhere in the flow field, the correct correspondence will not be obtained. The maximum displacement within the flow field may be determined by directly examining a superposition or overlay of the consecutive image frames.

Once the candidate subregion has been shifted to its identical frame 1 location ([25,25] within frame 2) and the candidate spots for correspondence to the original seed spot have been identified, a new subregion, the dynamic subregion, is shifted to the centroid pixel of *each* of the candidate spots. At each newly shifted position, the binary cross correlation coefficient is determined for the candidate spot pairs via

$$C_{ij} = \frac{\sum_{y,x=1}^{L} F_1^b \cap F_2^b}{\sqrt{\mathrm{B1} \times \mathrm{B2}}}, \qquad [2]$$

where the numerator represents the sum of the logical binary products between corresponding pixels in the subregions of frames 1 and 2. Once the size of the square candidate region is determined (based upon the maximum expected seed displacement within the image frame), the dynamic subregion may be automatically increased during the course of code execution. This feature yields better correlations, especially in regions of the image frame in which data may be sparse. Note, that in this example, the candidate subregion and the dynamic subregion are of the same size. F_1^b and F_2^b are the binary value at corresponding pixel positions within the dynamic subregion in frames 1 and 2, respectively, and L represents the number of pixels per side of the square dynamic subregion. The quantities B1 and B2 represent the total number of pixels of binary value 1 in the dynamic subregion in frames 1 and 2, respectively. Consider figure 2 again as an example. The sum of the logical products between the dynamic subregion in frame 1 and the dynamic subregion in frame 2 centered on candidate seed S is 2.0. The value of B1 is 10.0 and B2 is similarly 10.0. Hence, a C_{ij} value of 0.2 is obtained for a correspondence between seed spots A and S. However, the C_{ij} value for the dynamic subregion in frame 2 centered on seed A (pixel location 27,24) is 1.0, since the logical product is 10.0 and B1 = B2 = 10.0 as well. This represents a perfect correspondence. Hence, the correspondence between spot A in frame 1 and spot A in frame 2 is firmly established. In this manner, a similar procedure is conducted for all frame 1 spots. The corresponding seed spots in frame 2 are the ones which possess the greatest C_{ij} value per initial frame 1 spot. Once correspondence has been determined, the velocity of the particle or bubble is calculated based upon [1].

As discussed earlier in this paper, this correlation technique is used most efficiently on near-field flows. The affect of the expanding dynamic subregion thus creates a dilemma. Obviously, the dynamic subregion expansion must be limited to allow competent tracking. The dynamic subregion expands until it encompasses at least 5 spots. The solution is to keep the seed concentrations sufficiently that the dynamic region does not need to expand very much.

In actual flows, the largest values of the binary cross correlation coefficients (C_{ij}) will seldomly be 1.0. Thus, some degree of pattern variance between successive image frames can always be expected to occur. This phenomenon is exacerbated by highly three-dimensional turbulent flows which require a smaller Δt value in order for the fundamental assumption to be valid. Even slow-moving flows of high vorticity yield lower C_{ij} values compared with irrotational flow. As a result, various methods of double checking pair correspondence have been developed (Landreth & Adrian 1988). A double checking method is additionally applied in this cross correlation routine in which the total number of seed spots and pixel overlaps are summed for each possible seed pair over the entire image. In this manner, spots which repeatedly overlap in the course of full frame image analysis will possess higher "confidence" values than those for which overlaps seldomly occur (Yamamoto *et al.* 1989; Hassan *et al.* 1991).

This routine is run directly on a DEC VAX 8650 mainframe and completes most jobs (500–1000 spots) in <1 min CPU time. A series of two 1024×1024 image frames containing approx. 1000 spots can be processed quickly and analyzed with the spot finding and cross correlation algorithms. The flowchart describing image acquisition and analysis involving these schemes is illustrated in figure 3.

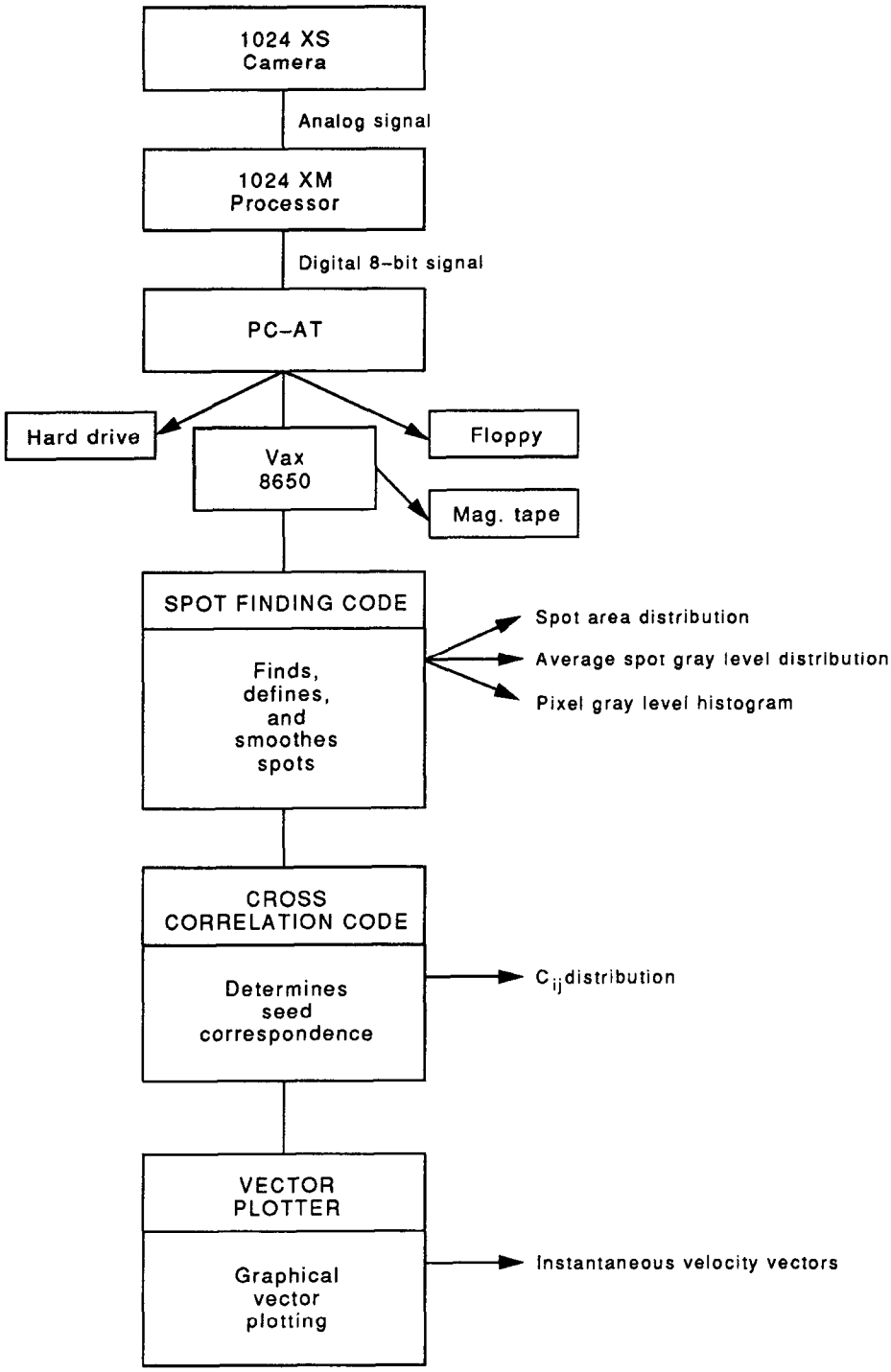

Figure 3. Flowchart for digital image acquisition and analysis.

Once particle correspondence is determined via the cross correlation algorithm, the instantaneous velocity vector between any two successive image frames may be plotted graphically. A final analysis routine utilizes a graphics package in order to display and plot the spot tracks as determined by the correlation program.

A method for interpolating scattered velocity data was implemented in order to produce a two-dimensional regular velocity vector grid from randomly spaced data sites. The interpolation

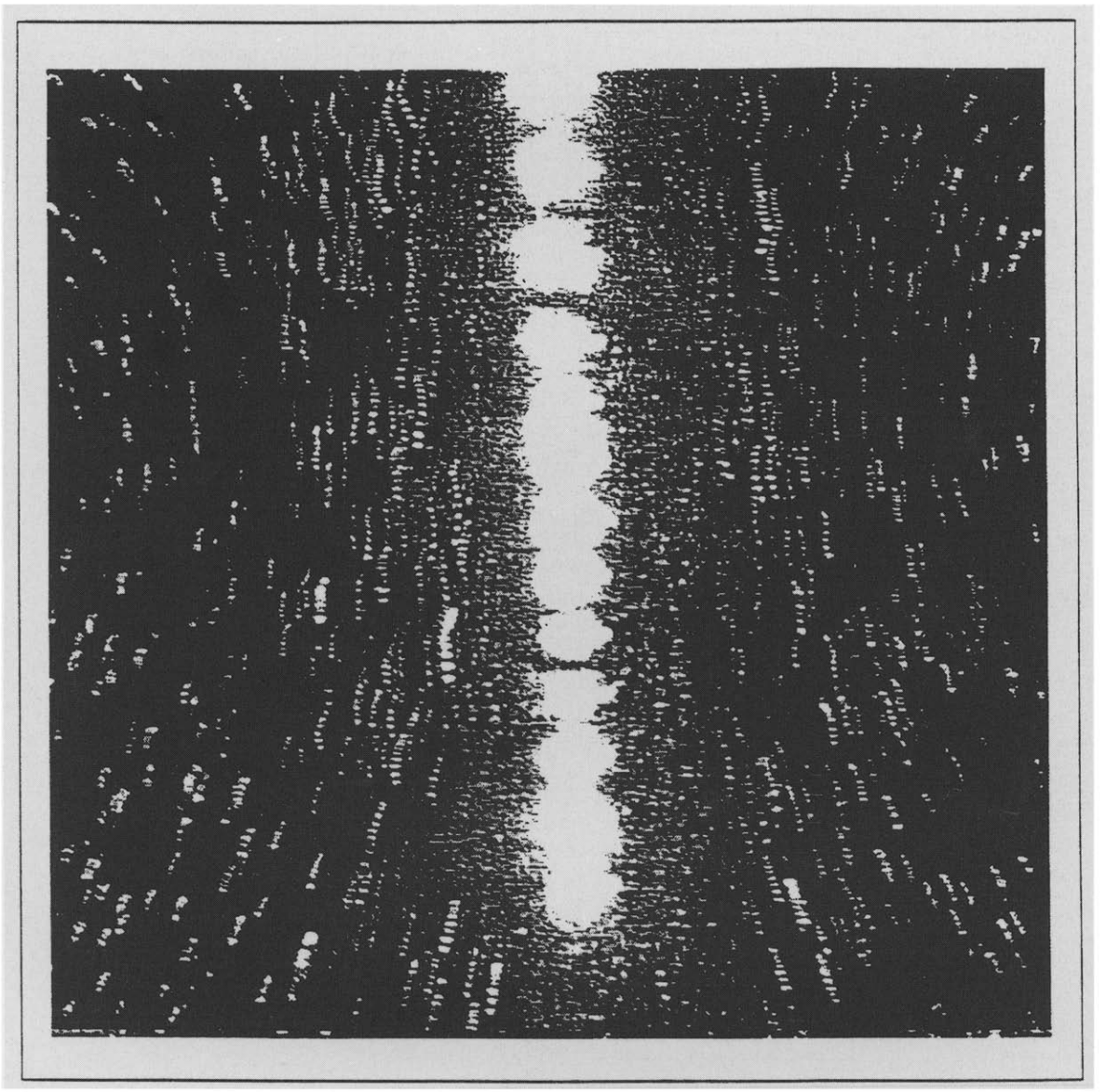

Figure 4. A 10-frame binary overlay depicting both bubble and induced particle motion.

method used was the Hardy multiquadratic scheme (Hardy 1971; Narcowich & Ward 1991; Hassan *et al.* 1991), whose basic relations are as follows:

$$\mathbf{V}_i = (u_i, v_i), \tag{3}$$

$$u_i(x_i, y_i) = \sum_{j=1}^{N} a_j \sqrt{1 + (x_i - x_j)^2 + (y_i - y_j)^2} \tag{4}$$

and

$$v_i(x_i, y_i) = \sum_{j=1}^{N} b_j \sqrt{1 + (x_i - x_j)^2 + (y_i - y_j)^2}, \tag{5}$$

where

$\mathbf{V}_i$ = the velocity vector at coordinates x_i, y_i,
u_i, v_i = the x and y components of $\mathbf{V}_i$,
N = the number of vectors to be used in the interpolation,

Figure 5. Frame 3 of the multiple bubble experiment (actual image).

$x_{i,j}, y_{i,j}$ = the coordinates of these vectors,

and

a_j, b_j = constants to be determined.

Applying the above relation, for the u or the v velocity component, will yield N coupled equations with N unknowns. The unknown constants, a_j and b_j, are subsequently determined by solving the linear system of equations. The constants are used in conjunction with the associated x_j and y_j values to reconstruct the velocity at any point in the flow field. This is done by substituting these values into the above relations [3–5] at the x_i and y_i coordinates of interest.

Initial results from the cross correlation routine produce some vectors which are obviously incorrect. Using a C_{ij} value to eliminate these "wrong" vectors can be used. However, the use of such a limiting value decreases the total number of vectors plotted at the expense of achieving a greater reliability in the results of the cross correlation process. Thus, a compromise must be

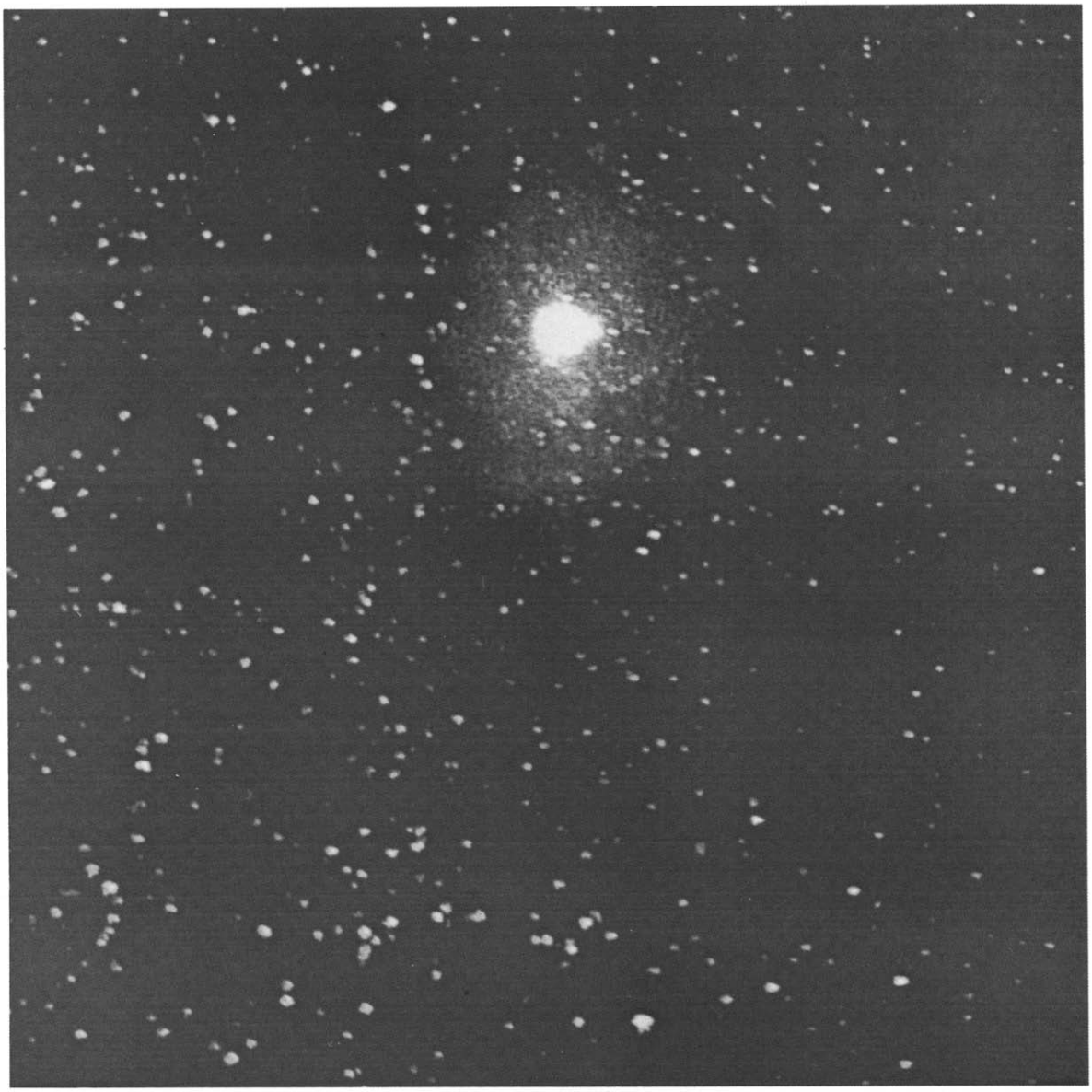

Figure 6. Frame 8 of the single bubble experiment (actual image).

reached in a trial-and-error fashion between the number of vectors which can be displayed and the desired confidence level of obtained velocities. A method of "cleaning" the data based on suggestions from Landreth & Adrian (1988) was developed. This process involves using the interpolated field produced by the best vectors (i.e. the vectors with the highest C_{ij} values), and adding the vectors from the original data which closely match this field.

Utilizing the interpolated, two-dimensional instantaneous velocity fields obtained from the Hardy approach (cf. [3]–[5]) the vorticity maps of the data were calculated via

$$\zeta = \nabla \times \mathbf{V} = \left(\frac{\partial v}{\partial x} - \frac{\partial u}{\partial y}\right)\mathbf{k}, \qquad [6]$$

where

u = the x or horizontal component of the velocity field $\mathbf{V}$,

v = the y or vertical component

and

ζ = the z component of the vorticity field.

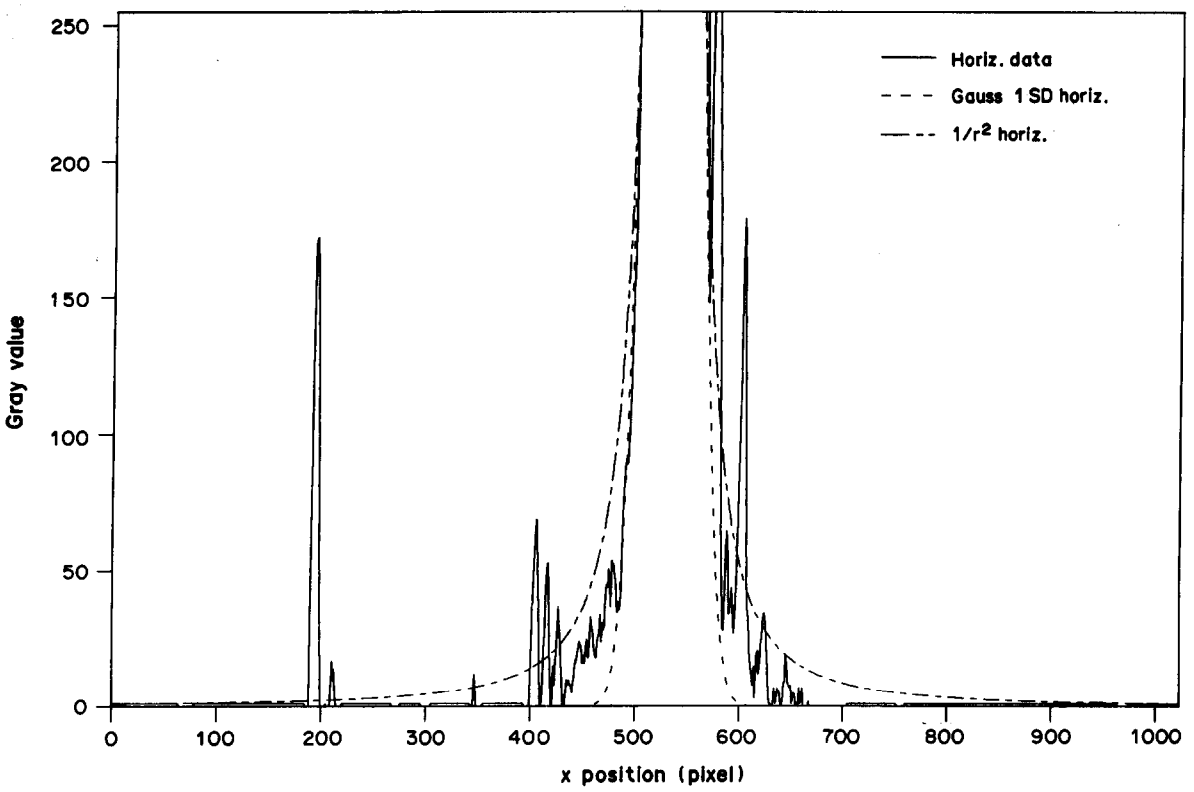

Figure 7. Gray level distribution along a horizontal line and threshold functions.

3. RESULTS

The following results describe the application of the current PIV method to the study of a gas agitated mixing flow within a rectangular vessel.

3.1. Preliminary image processing and analysis

Figure 4 illustrates a 10-frame overlay depicting the rise of a train air bubbles within a seeded mineral oil. This figure was produced by setting all pixels whose gray level was >30 to equal 255, and those <30 to equal 0 (i.e. a binary image). The effects of the buoyancy-induced flow on the surrounding seeded liquid are evident as the seed particles appear to have been upwardly entrained within the wakes of the passing bubbles. The actual flow field of figure 4 consisted of two rising gas bubbles whose relative locations are better illustrated in figure 5. This latter figure (actual image with no threshold applied) corresponds to the third image in the 10-frame series. An important feature to note with regard to figure 5 is the large circular halo or corona extending from the bubbles themselves. These circular areas of increased gray level intensity are associated with direct laser light reflection from the surfaces of the bubbles. The reflection is significant as the coronas extending from each bubble's center actually meet and join, thus creating a substantial region of elevated gray levels. This effect had immediate consequences with regard to initial analysis attempts. Specifically, the individual bubbles could not be distinguished as separate entities by the spot finding algorithm. In fact, the entire central region of each image frame was identified by the algorithm as a single spot consisting of over 100,000 pixels when a global threshold of 30 was applied. Obviously, some sort of local thresholding was required in order to restrict the reflection halos associated with each bubble to the extent that individual bubbles could be identified and tracked. An additional concern extended beyond that of just identifying separate bubbles however; the seed particles surrounding each bubble had to be held intact throughout any applied thresholding operation in order to fully and properly characterize the flow field in the near-bubble regions.

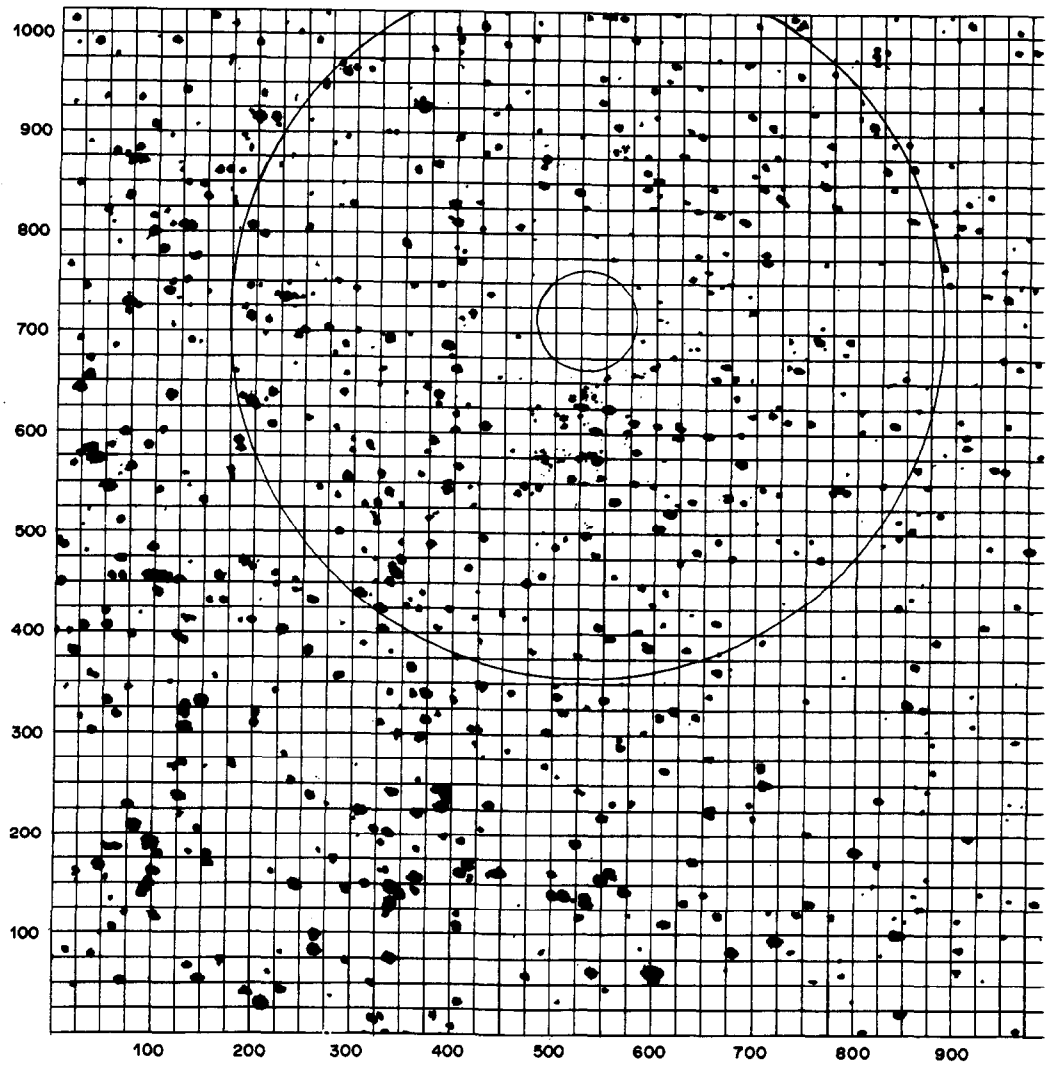

Figure 8. Radial effect of the $1/r^2$ threshold function.

A simple answer to the bubble reflection problem would have been to repeat the image acquisition at a lower laser energy output such that bubble reflection halos were proportionally reduced. In fact, this was initially attempted. Although reduction in laser power did eliminate the bubble halo effect, it resulted in an inability to properly illuminate the actual seed particles whose scattering properties require substantial laser energy. Another possible solution was to use a higher threshold. A global threshold of 100 was applied to the image. This procedure effectively eliminated the problems associated with bubble reflection and separate bubbles could now be distinguished. However, the extent of thresholding required to achieve this effect resulted in substantial seed dropout in regions of the image plane external to the corridor through which the gas bubbles rise. Particles within the central regions of the image plane, however, were still intact despite implementation of the threshold operation. This is the result of increased illumination due to reflection from the bubble surface. Thus, the final solution to the problem was met by applying a local threshold function.

Figures 6–8 are used to illustrate the threshold function. Figure 6 shows a single gas bubble emitted into a previously quiescent working fluid. Analysis of the gray level data on a horizontal line drawn through the bubble centroid is shown in figure 7. Most of the values on this line are close to zero, corresponding to the background. The bubble region is characterized by the wide band of pixels (gray level 255) centered on pixel position 530. The spike in the data are produced

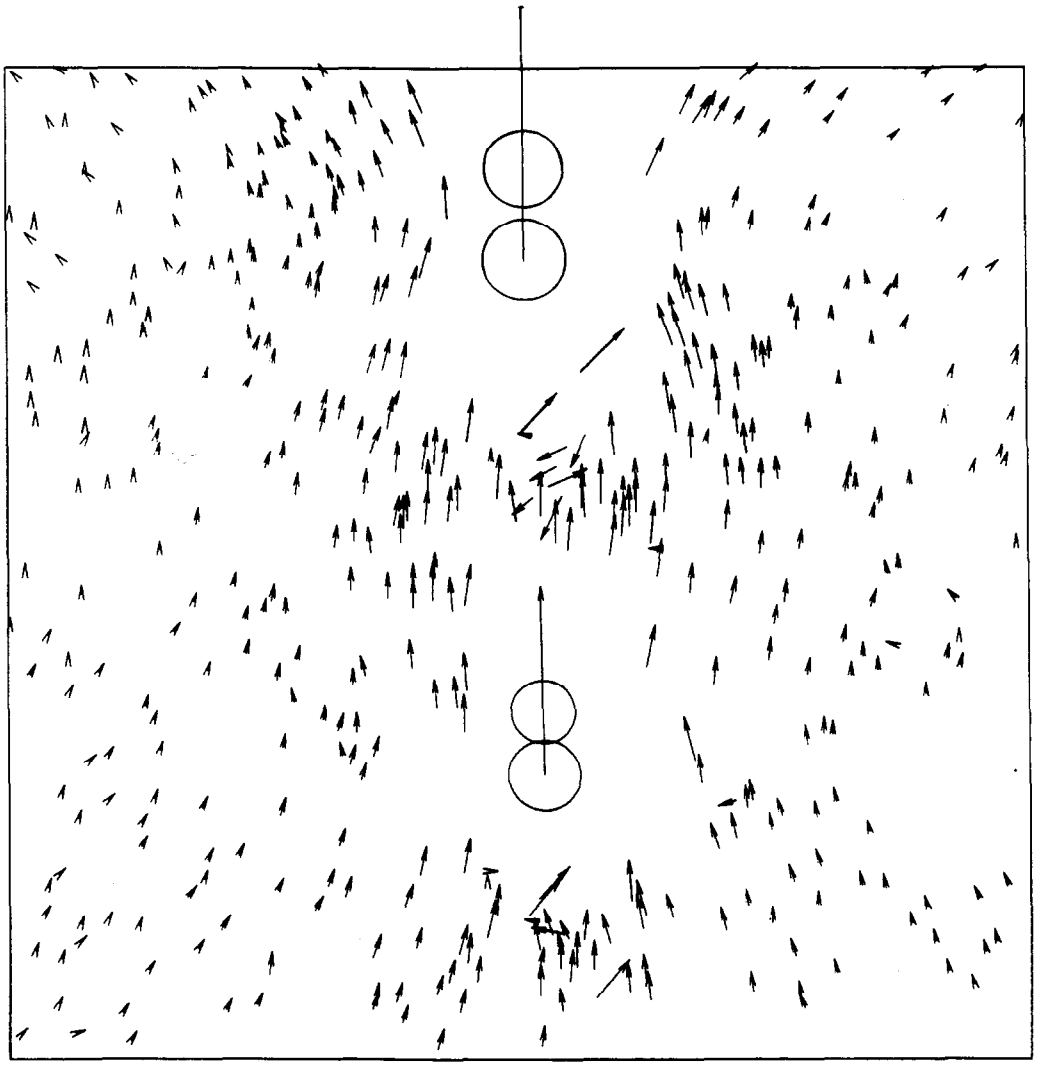

Figure 9. Particle and bubble velocity vectors resulting from a chain of rising air bubbles.

by the tracer seeds. Various methods of local thresholding were examined to determine the proper function to distinguish the seeds in the corona. A Gaussian function (1 standard deviation) and a $1/r^2$ function, centered at the bubble, are shown in figure 7. The authors determined that the $1/r^2$ function fitted the data best, and was used as the threshold function. Figure 8 shows the results of applying a background threshold of 5 along with the $1/r^2$ function at the bubble location. All gray levels above values were plotted. All the data in the bubble region (inner circle, radius = 50) was removed. The $1/r^2$ function was applied between the inner and outer circles. The outer circle depicts the point where the function reached the background threshold.

3.2. Image analysis using a cross correlation technique

The next step in the image analysis process was to determine the particle correspondence between successive image frames. The cross correlation routine discussed previously was implemented for this purpose. The results of the point-by-point digital analysis of the current data are displayed in figure 9. This figure portrays the instantaneous velocity vectors obtained corresponding to particle and bubble motion between image frames 3 and 4 of the 10-frame sequence. The vectors are drawn from the centroid in the starting frame (tail) to the centroid of the same spot in the following frame (head). A velocity scaling factor of 3 was used for all vector plots. The locations

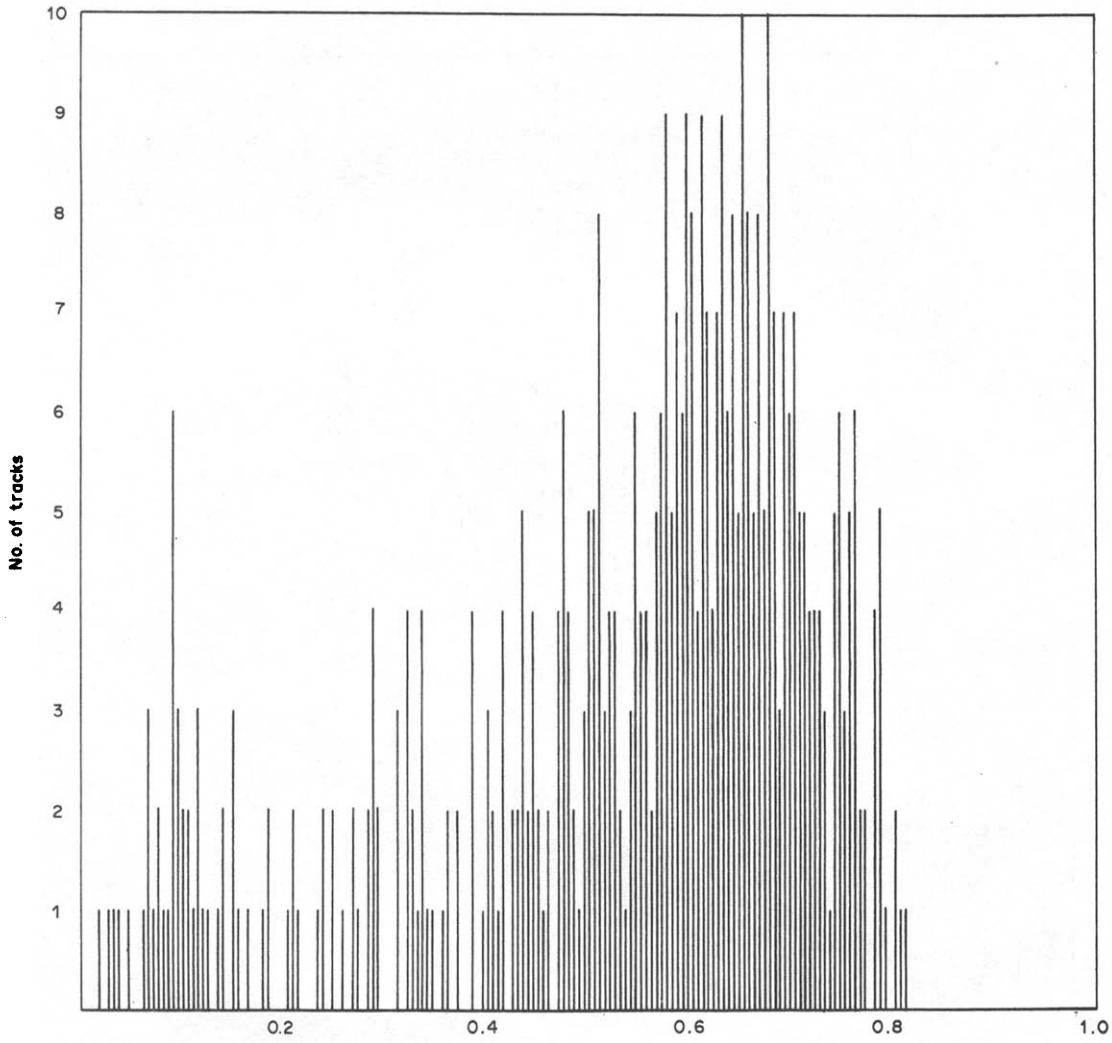

Figure 10. C_{ij} value distribution of the vectors in figure 9 (cf. [5]).

of the two bubbles are drawn corresponding to their positions in image frames 3 and 4. Figure 9 is the velocity map obtained when a binary cross correlation coefficient (C_{ij}) limiting value is not specified. In other words, all vectors are displayed regardless of the strength of their correlation. Specification of a C_{ij} limiting value may be applied in order to plot only vectors which have a cross correlation coefficient which exceeds the specified value.

The C_{ij} values for all vectors in figure 9 are illustrated in figure 10. This is a fairly low distribution for the binary cross correlation coefficients considering that ideal spot correspondence would have a C_{ij} value of 1.0. This phenomenon validates the previously mentioned assertion that rotational or three-dimensional flows will be characterized by less than ideal correlation values. This is due to the fact that the characteristic grouping of seeds within such flows has a tendency to degrade at a faster rate than in the case of irrotational flows. Had a smaller time interval Δt been chosen for image acquisition, less degradation of seed grouping would have occurred and hence correlation values would be generally greater. Estimates of the accuracy of velocities obtained by this tracking method and affects of Δt and seed concentration have been determined (Hassan *et al.* 1991).

Figure 11 displays the results of applying the cleaning technique to figure 9. The C_{ij} value chosen to begin the cleaning was equal to 0.5. Figure 12 depicts the interpolation of the instantaneous velocities obtained in figure 11.

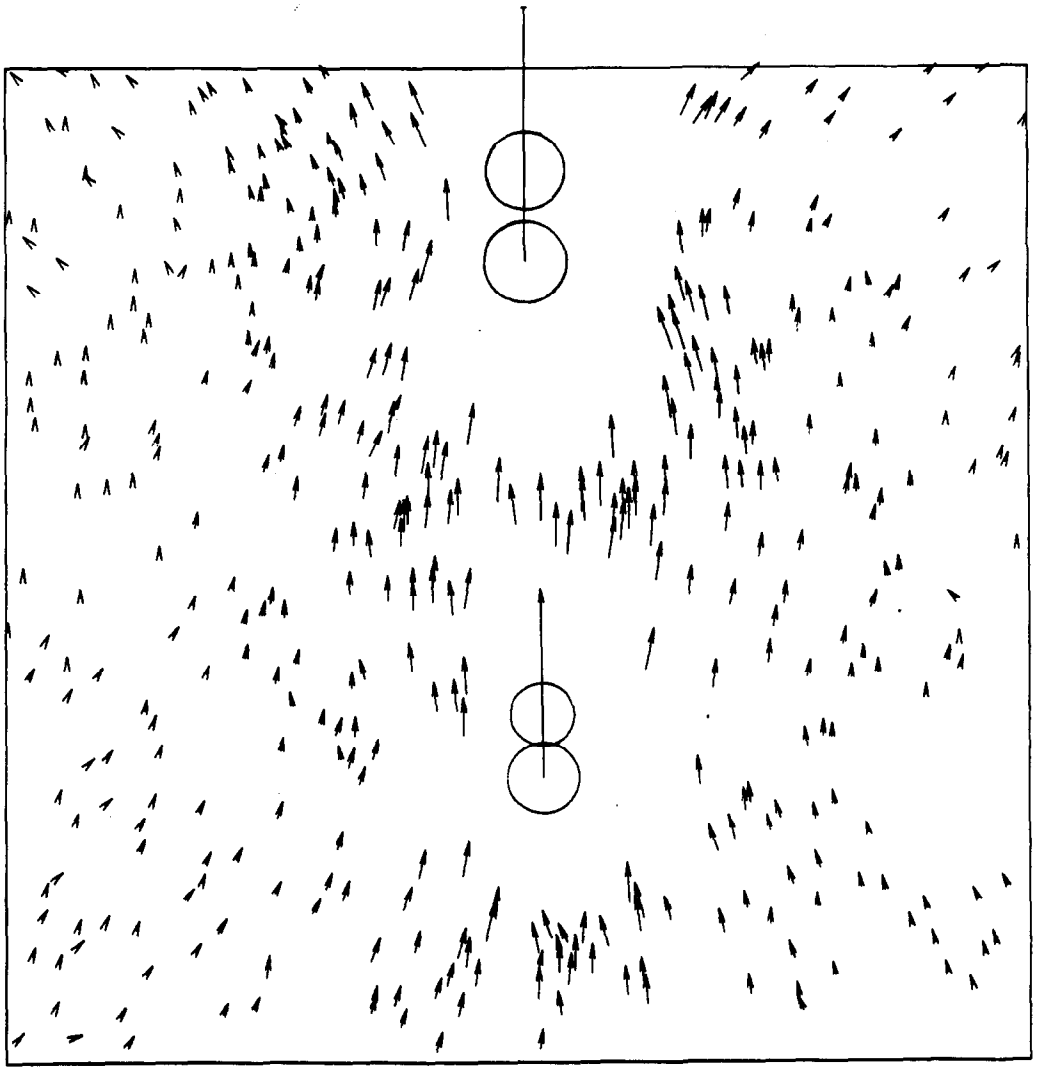

Figure 11. Particle and bubble velocity vectors (after cleaning figure 10).

Although the current state of digital imaging technology prohibits the required image acquisition rate necessary in order to study turbulent microscale structure, the current method allowed the temporal velocity fluctuations at a given point within the flow field to be obtained on a timescale corresponding to frame rates utilized in this analysis. Figure 13 represents the 25 × 25 mm flow field for which the present analysis was conducted illustrating the relative positions of the two rising gas bubbles at their approximate locations within each frame of the 10-frame series. The point indicated is one for which the temporal x and y components of the velocity field (u and v, respectively) were obtained based on interpolated data from each analyzed image frame. The measurement point illustrated in figure 13 is located 11.523 mm to the right and 9.814 mm above the lower left-hand corner of the 25 × 25 mm square region. This point was representatively selected since velocity data was always obtained in this region throughout the 10 image frames. Figure 14 displays the temporal variation in the x and y velocity components of the working fluid at the measurement point indicated. As indicated in figure 14, the x component of the temporal velocity vector (u direction) at the measurement point is initially negative as the lower bubble approaches the point, and then quickly takes on a positive value as a passing bubble entrains liquid into its wake. Additionally displayed is the position of the lower bubble relative to the measurement point. Note that the maximum vertical velocity component occurs at $t = 0$, since the fluid at the

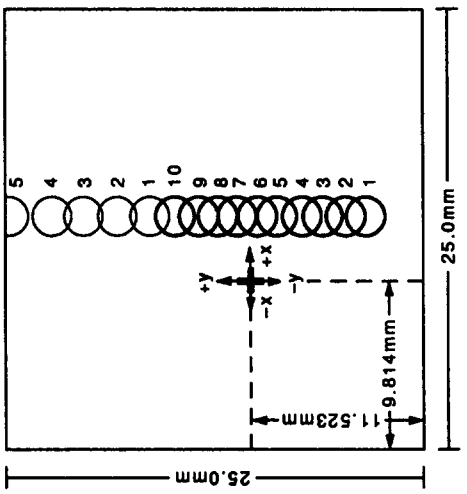

Figure 13. Location of the measurement point for velocity fluctuation.

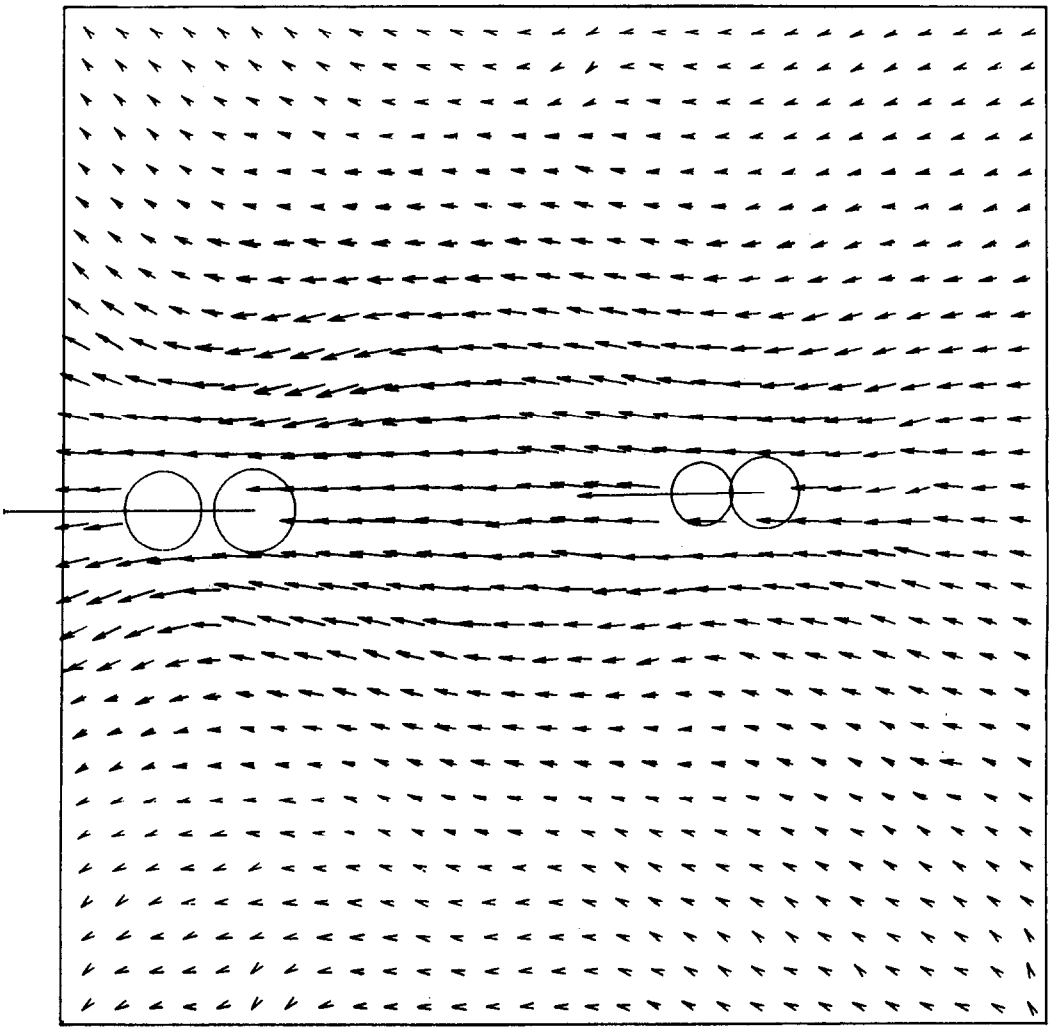

Figure 12. Interpolated particle and bubble velocity field based upon seed motion in figure 11.

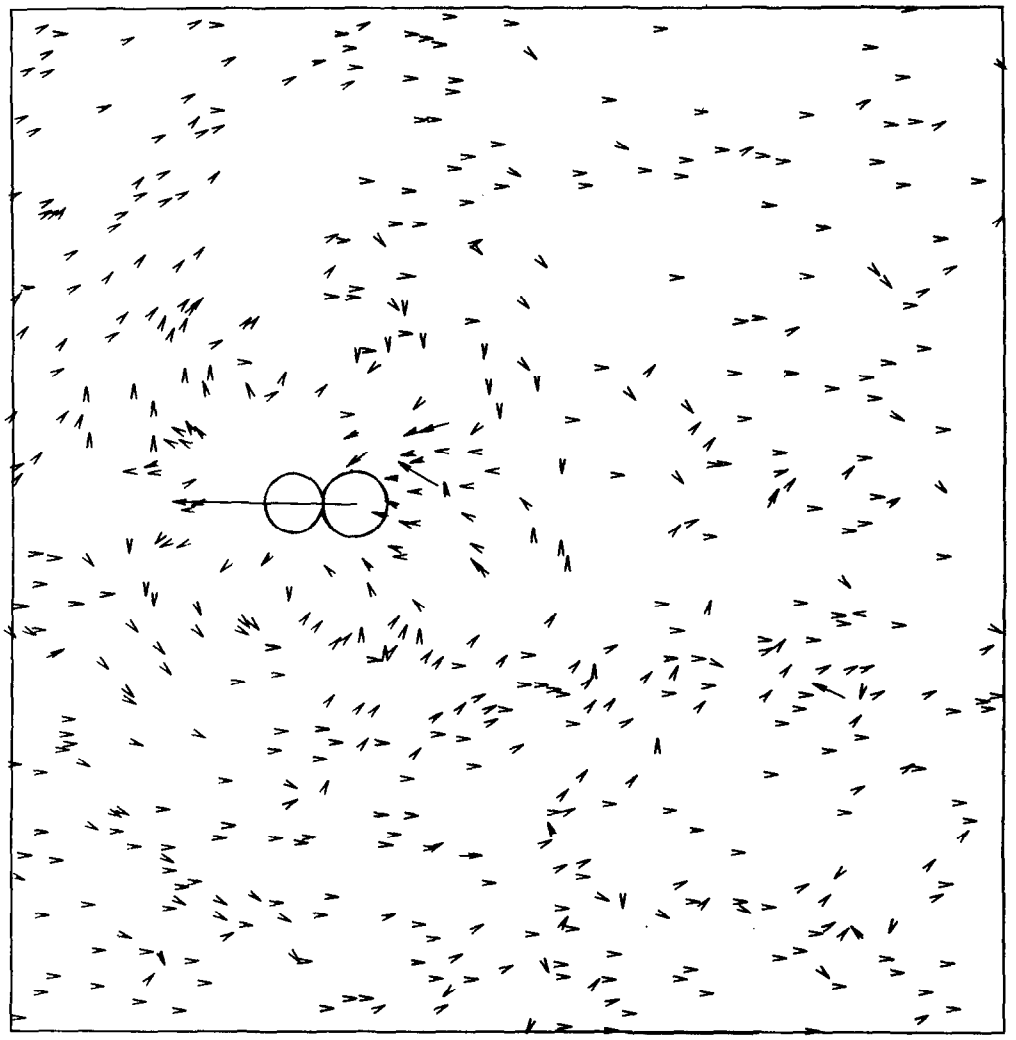

Figure 15. Particle and bubble velocity vectors resulting from a single bubble rising into a quiescent medium.

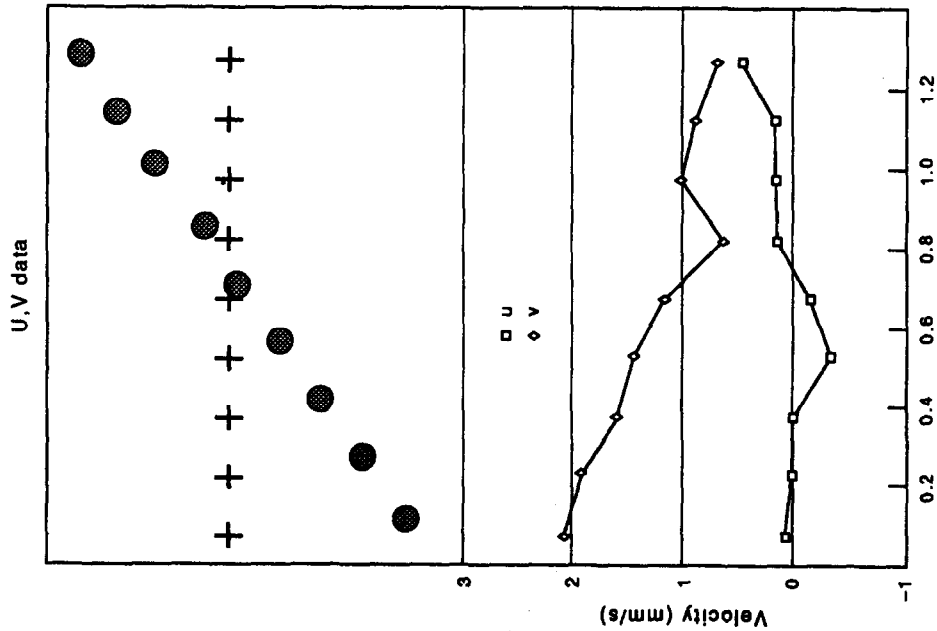

Figure 14. Temporal velocity fluctuation and relative bubble location at the point indicated in figure 13.

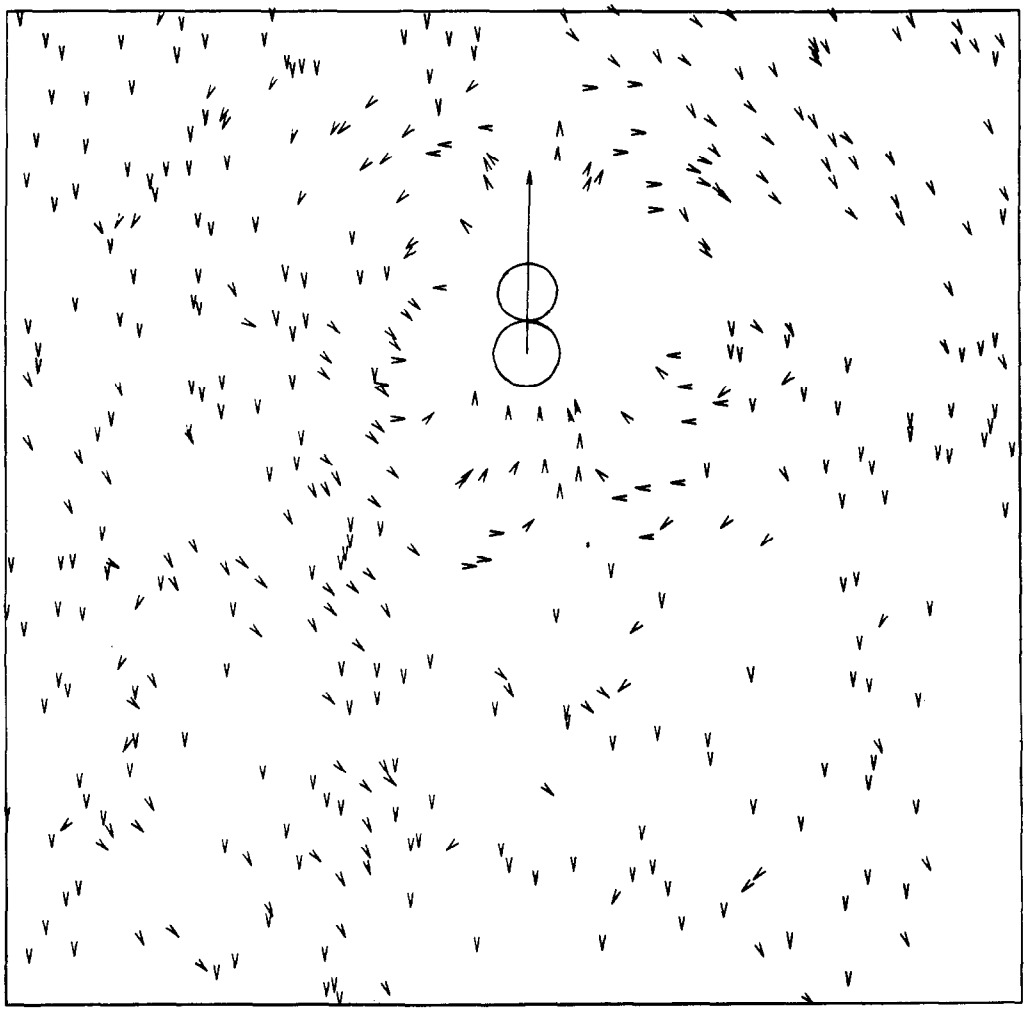

Figure 16. Frame 8–9 velocity vectors (after cleaning figure 15).

indicated point is affected by the entraining wake of the upper bubble and the advance of the lower bubble.

In slight contrast to the data previously analyzed and discussed, figures 15 and 16 depict the results of the single gas bubble dataset (figure 6). The fluid flow speed for this image was much slower than the speed of the rising bubble. Figure 16 shows the instantaneous velocity vectors produced after the cleaning process using a C_{ij} value of 0.5. In this case the working fluid has not been affected by previously risen bubbles; hence, the fluid motion is characterized by a general downward flow around the surface of the rising bubble with entrainment and local recirculation immediately behind the bubble's lower surface. Some of these downward vectors could be caused by particle settling, however, no major particle settling was noted in other images. Figure 17 depicts the interpolated field. Note, there may be regions in an interpolated vector field which may be inaccurate due to regions without data, or with incorrect data. Figures 18 and 19 depict the streamlines and vorticity profile based upon the interpolated data of figure 12. Figures 20 and 21 depict the particle rake trace and vorticity profile based upon figure 17.

In the particle velocity estimation technique described in this work, one starts by estimating the centroid location of all particles. The centroids are computed with some level of accuracy. The velocity estimates are obtained by computing the differences between respective particle centroids, and are thus affected by the practice centroid estimates. The error from the centroid estimation propagates to the velocity estimation. The interpolation operation adds an additional error source to the regularized velocity vector field. Finally, the vorticity field is computed, which is now a second-order derivative of the initial particle position. The quality of the vorticity calculation is

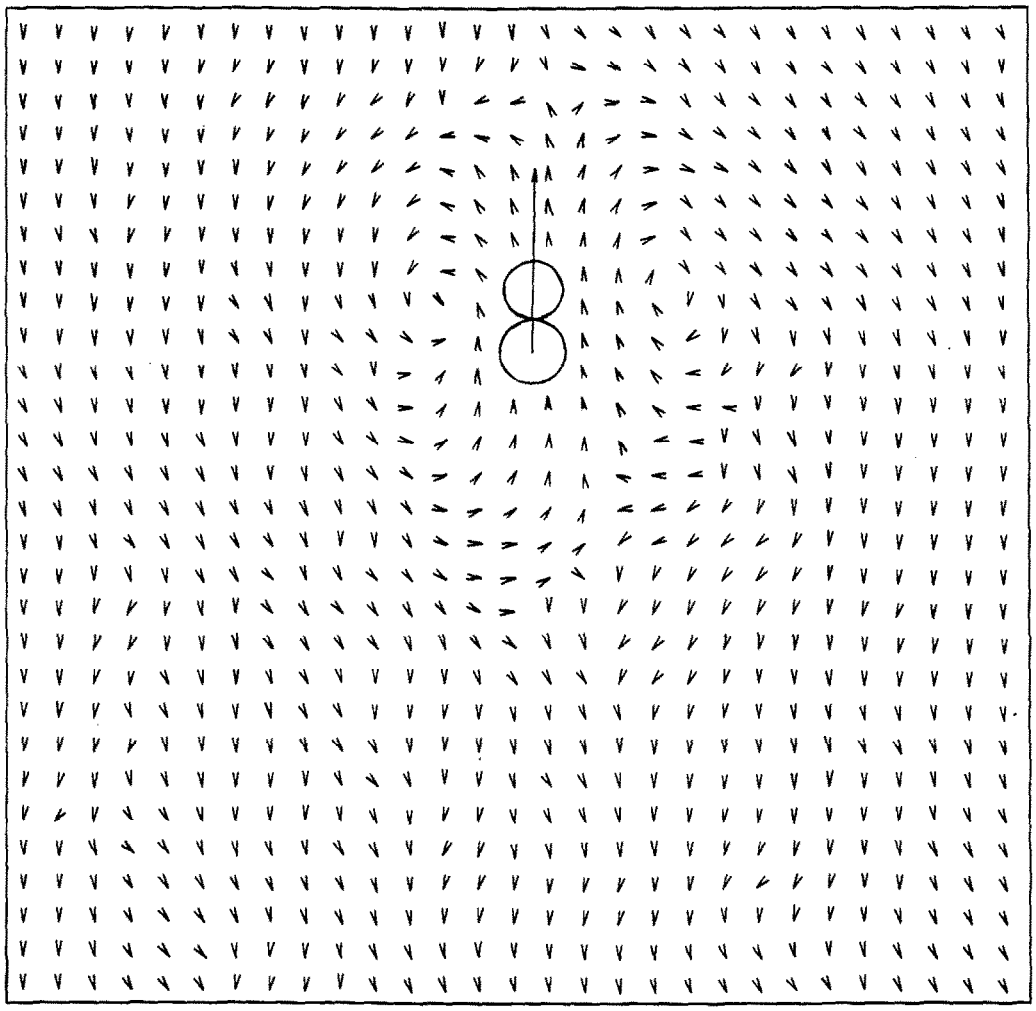

Figure 17. Interpolated field of figure 16.

directly related to the initial particle position estimates, and subsequent velocity estimates. The error in the velocity estimates are proportional to the inverse of the particle displacement between exposures. Assuming the particle centroids are determined to ± 1 pixel, and displacements are between 2 and 10 pixels, then the relative error in the velocity estimates is on the order of $\frac{1}{10}$–$\frac{1}{2}$ or 10–50%. Hence, the vorticity field estimated must have errors in the range of 14–70% r.m.s. Caution must be used in computing second-order flow statistics from moderate to low accuracy first-order statistics.

The ability of the routines implemented above to accurately determine the spot correspondence between successive image frames has been verified using both synthetically generated spot data and experimental single-phase data (Hassan *et al.* 1991). However, numerous sources of error have yet to be fully quantified. Potential errors associated with this experiment involve the processes of spot centroid determination; the operator intervention often required in the C_{ij} thresholding procedure; and uncertainties associated with data loss or "dropout" due to three-dimensional fluid motion. Although fully digitial imaging and analysis methods offer speed and convenience, mean bias errors from low video resolution may arise as well as other forms of random errors associated with anomalies in the image acquisition process (Prasad *et al.* 1990).

4. CONCLUSIONS

Since its inception as a tool for fluid velocity measurement, the technique of PIV has repeatedly demonstrated its significant merits among methods currently available in the study of experimental

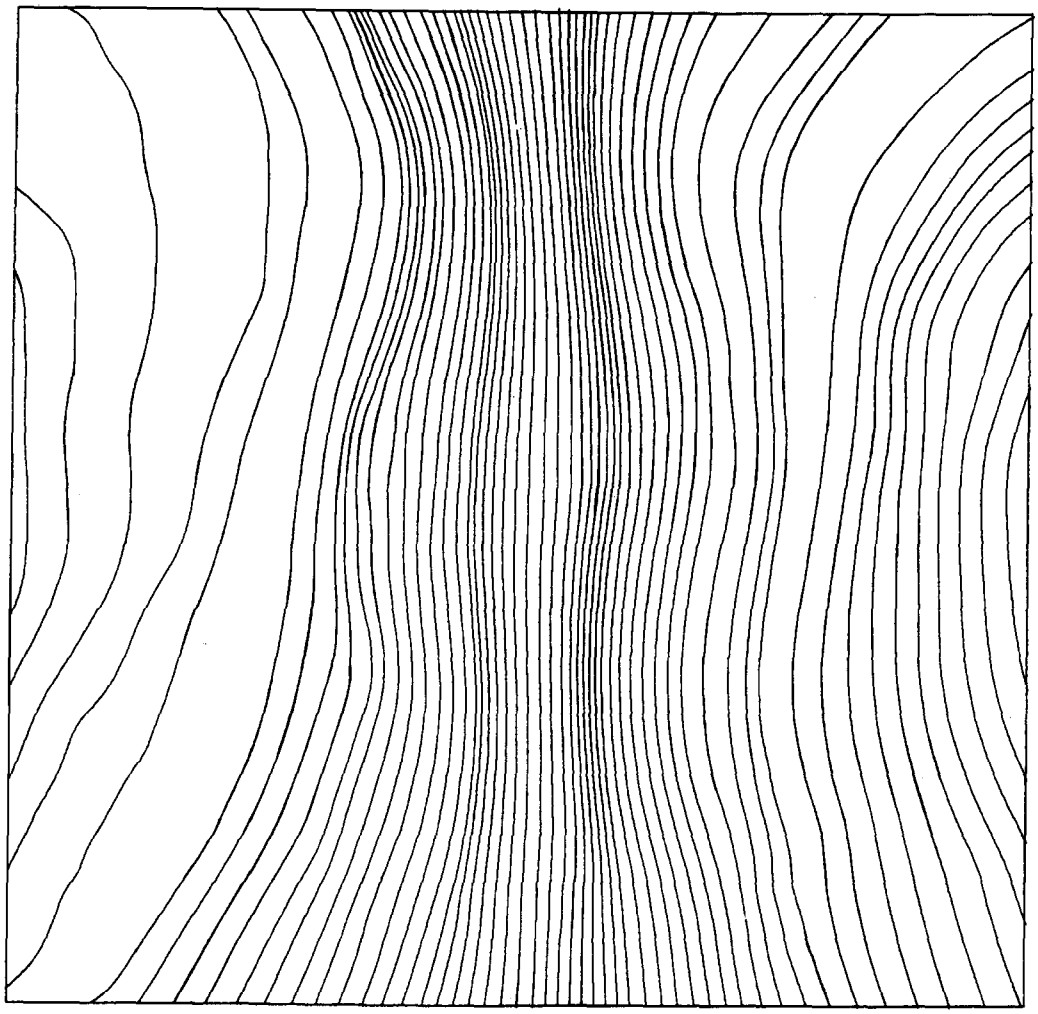

Figure 18. Streamlines based on the interpolated velocities of figure 12.

fluid flow systems. Although the technique is a relatively recent contributor to the available methods for experimental fluid system analysis, it has nevertheless succeeded in substantiating its capacity to provide quantitative fluid velocity information in such a manner that several advantages can be realized over more traditional methodologies. Namely, PIV has the capability to acquire instananeous full-field velocity data in a single measurement such that the flow itself remains undisturbed by the measurement. The method has proven its effectiveness in providing quantitative fluid velocity information over a large range of single-phase flow regimes in an increasing variety of engineering systems; however, the technique is just beginning to demonstrate its applicability to the full-field non-invasive analysis of two-phase systems.

Although the majority of PIV laboratories rely upon image capture involving photographic media as well as related opto-mechanical analysis techniques, continual advances in the field of imaging have allowed the authors to construct and effectively utilize a completely digital image capture and analysis facility. Fully digital image and analysis schemes avoid much of the complexities associated with photographic image processing, such as ambiguities associated with superimposed fields on single doubly-exposed image frames and direction of particle travel uncertainties (Adrian 1991). However, disadvantages are also present in the form of lower resolution and the large Δt (between frames) constraints associated with standard video imaging systems.

In this study, digital image data was acquired of a dispersed air bubbly flow and its effects upon a surrounding mineral oil working fluid within a transparent enclosure. A point-by-point

Figure 19. z-Component of vorticity. Gas bubble in mineral oil. Experiment c34.

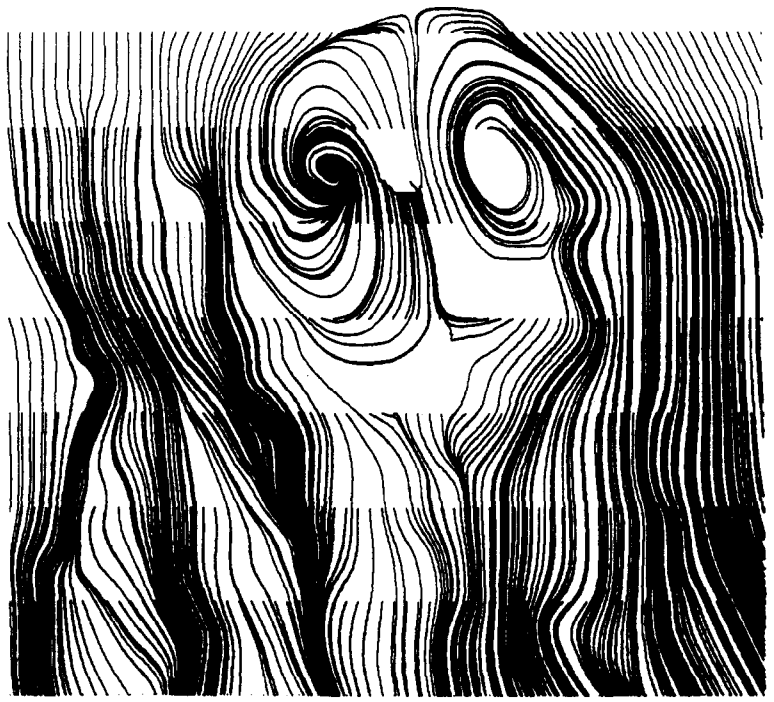

Figure 20. Particle trace based on the interpolated velocities of figure 17. Gas bubble in mineral oil. Experiment 89.

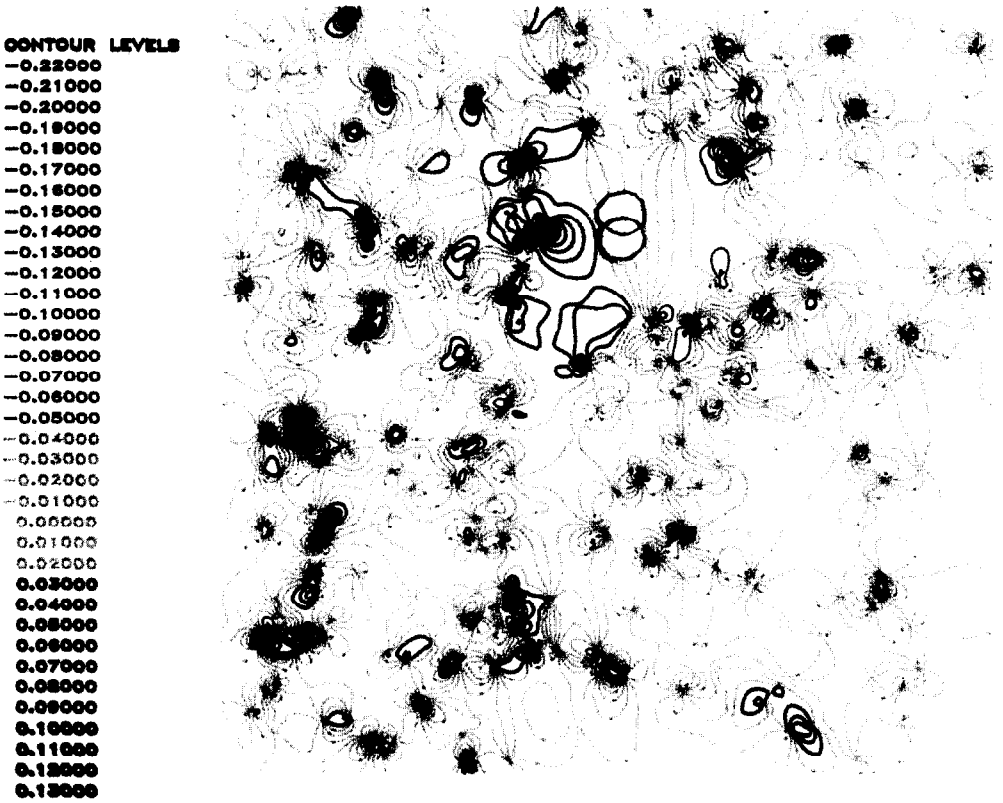

Figure 21. z-Component of vorticity. Gas bubble in mineral oil. Experiment b89.

digital cross correlation analysis algorithm was employed in order to obtain the full-field instantaneous velocity profiles of both liquid and gaseous components of a simple two-phase system. Additionally, the temporal velocity fluctuation of the liquid phase induced by the rising bubble motion were measured at a given point. The potential of the PIV technique for use in the further detailed study of multicomponent flows has been demonstrated, specifically with regard to its capability to quantify relative component velocities upon which parameters such as interfacial drag and flow regime characterization are dependent. The desire to develop a complete understanding of two-phase flows depends largely upon this ability to fully characterize them.

REFERENCES

ADRIAN, R. J. 1986a Multipoint optical measurements of simultaneous vectors in unsteady flow—a review. *Int. J. Heat Fluid Flow.* **7,** 127–145.

ADRIAN, R. J. 1986b Image shifting technique to resolve directional ambiguity in double-pulsed velocimetry. *Appl. Opt.* **25,** 3855–3858.

ADRIAN, R. J. 1991 Particle-imaging techniques for experimental fluid mechanics. *A. Rev. Fluid Mech.* **23.**

ADRIAN, R. J. & LANDRETH, C. C. 1988 Overview of particle image velocimetry. *Laser Top.* **Spring,** 10–13.

CANAAN, R. E. 1990 Full-field velocity measurements of single and two phase flows using digital pulsed laser velocimetry. M.S. Thesis, Texas A&M Univ., College Station, TX.

DUDDERAR, T. D., MEYNART, R. & SIMPKINS, P. D. 1988 Full field laser metrology for fluid velocity measurement. *Opt. Lasers Engng* **9,** 163–199.

HARDY, R. L. 1971 Multiquadric equations of topography and other irregular surfaces. *J. Geophys. Res.* **76,** 1905–1915.

HASSSAN, Y. A., BLANCHAT, T. K. & HILD, R. D. 1990 Full-field imaging technique using high-energy pulsed laser velocimetry. *Conf. on Imaging Algorithms and Techniques: SPIE/SPSE Proc.* **1244,** 130–142.

HASSAN, Y. A., BLANCHAT, T. K. & SEELEY, C. H. JR 1991 PIV flow visualization using particle tracking techniques. *Measur. Sci. Technol.* Submitted.

HILD, R. D. 1989 Single phase flow visualization using pulsed laser velocimetry. Master's Thesis, Texas A&M Univ., College Station, TX.

KIMURA, I. & TAKAMORI, T. 1986 Image processing of flow around a circular cylinder by using correlation technique. *Flow Visual.* **IV,** 221–226.

KIRITSIS, N. 1989 Statistical investigation of errors in partial image velocimetry. M.S. Thesis, The Ohio State Univ., Columbus, OH.

LANDRETH, C. C. & ADRIAN, R. J. 1988 Measurement and refinement of velocity data using high image density analysis in particle image velocimetry. Presented at *Applications of Laser Anemometry to Fluid Mechanics—Fourth Int. Symp.*, Lisbon, Portugal, pp. 484–497.

LOURENCO, L. M. & KROTHAPALLI, A. 1987 The role of photographic parameters in laser speckle or particle image displacement velocimetry. *Expts Fluids.* **5,** 29–32.

NARCOWICH, F. J. & WARD, J. D. 1991 Norms of inverses and condition number for matrices associated with scattered data. *J. Approx. Theory* **64,** 69–94.

PRASAD, A. K., ADRIAN, R. J., LANDRETH, C. C. & OFFUT, P. W. 1990 Effect of resolution on the speed and accuracy of particle image velocimeter interrogations. In *Proc. Twelfth Symp. on Turbulence*, Rolla, MO, pp. B14-1–B14-10.

SALCUDEAN M. & LAI, K. Y. M. 1988 Computation of three-dimensional flow associated with heat and mass transfer in gas-agitated liquid reactors. *Numer. Heat Transfer.* **14,** 97–111.

SIMPKINS, P. G. & DUDDERAR, T. D. 1978 Laser speckle measurement of transient Bernard convection. *J. Fluid Mech.* **89,** 665–671.

UEMURA, T., IGUCHI, M., KAWABATA, H. & MORITA, Z. 1990 Velocity measurements in a gas injection vessel using multi-particle tracking method. In *Proc. Sixth Int. Iron and Steel Congress 1990*, Nagoya, Japan, pp. 61–66.

VAN DYKE, M. 1982 *An Album of Fluid Motion.* The Parabolic Press, Stanford, CA.

YAMAMOTO, F., DAI, Y., KOUKAWA, M., ITOH, M. & UEMURA, T. 1989 Numerical simulation on error analysis in particle tracking velocimeter by correlation method. In *Flow Visualization—1989*, Vol. 85, pp. 9–14. ASME, New York.